The Astrophysical Journal, 658:643–656, 2007 March 20

PROPERTIES OF SOLAR POLAR CORONAL PLUMES CONSTRAINED BY ULTRAVIOLET CORONAGRAPH SPECTROMETER DATA

N.-E. Raouafi,[1] J. W. Harvey,[1] and S. K. Solanki[2]
Received 2006 August 10; accepted 2006 October 13

ABSTRACT

We investigate the plasma dynamics (outflow speed and turbulence) inside polar plumes. We compare line profiles (mainly of O VI) observed by the Ultraviolet Coronagraph Spectrometer (UVCS) instrument on *SOHO* at the minimum of solar cycle 22–23 with model calculations. We consider Maxwellian velocity distributions with different widths in plume and interplume regions. Electron densities are assumed to be enhanced in plumes and to approach interplume values with increasing height. Different combinations of the outflow and turbulence velocity in the plume regions are considered. We compute line profiles and total intensities of the H I Lyα and the O VI doublets. The observed profile shapes and intensities are reproduced best by a small solar wind speed at low altitudes in plumes that increases with height to reach ambient interplume values above roughly 3–4 $R_\odot$, combined with a similar variation of the width of the velocity distribution of the scattering atoms/ions. We also find that plumes very close to the pole give narrow profiles at heights above 2.5 $R_\odot$, which are not observed. This suggests a tendency for plumes to be located away from the pole. We find that the inclusion of plumes in the model computations provides an improved correspondence with the observations and confirms previous results showing that published UVCS observations in polar coronal holes can be roughly reproduced without the need for large temperature anisotropy. The latitude distributions of plumes and magnetic flux distributions are studied by analyzing data from different instruments on *SOHO* and with SOLIS.

Subject headings: line: profiles — plasmas — scattering — solar wind — Sun: corona — Sun: magnetic fields — turbulence

1. INTRODUCTION

This paper is a forward-modeling investigation of the plasma dynamics of polar plumes. These so-called polar rays or polar plumes (e.g., van de Hulst 1950; Saito 1958; Harvey 1965; Koutchmy, 1977; DeForest et al. 1997) trace open magnetic field lines to different heights depending on observation type. In extreme ultraviolet (EUV) emission line spectroheliograms, plumes appear as short spikes near the polar limb (Bohlin et al. 1975a; Ahmad & Withbroe 1977; Widing & Feldman 1992; Walker et al. 1993), with unchanged shape and sudden brightness changes over typical lifetimes ranging from several hours to days (see DeForest et al. 1997; Del Zanna et al. 1997). EUV observations can be used to characterize the bases of polar plumes, and also their plasma characteristics (densities, temperatures, flows, abundances, etc.) and also other processes, such as heating and wave propagation (e.g., Bohlin et al. 1975b; Walker et al. 1988, 1993). Soft X-rays show mainly the hot plasma at the footpoints of the plumes (e.g., Ahmad & Webb 1978), which are also seen as weak radio sources (Gopalswamy et al. 1992). DeForest et al. (1997, 2001b) have shown that most white-light polar rays can be directly associated with the EUV polar plumes and their footpoints on the solar surface.

Above the solar limb, polar plumes appear brighter than the surrounding media, suggesting that they are denser than the background corona or interplume regions (e.g., van de Hulst 1950; Saito 1958, 1965). The coronal-background electron density is about $\sim 10^8$ cm^{-3} and falls sharply with height (see different density models in Raouafi & Solanki 2006). In comparison, the density of polar plumes ranges from 10^8 to 10^{10} cm^{-3} (Del Zanna et al. 1997; Young et al. 1999). Young et al. (1999) reported electron densities corresponding to the strong brightenings at plume footpoints of the order of $(2.5-5.6) \times 10^9$ cm^{-3} and found no decrease with height up to 70 Mm. They also inferred temperatures of the order of 2 MK. In a recent publication, Wilhelm (2006), using off-limb spectroscopic measurements from the spectrometer SUMER (Wilhelm et al. 1995) on board *SOHO* (Domingo et al. 1995), found that plumes are approximately 5–6 times denser than interplume regions up to $\approx$1.2–1.3 $R_\odot$. The plume-interplume density ratio changes little in this height range. Note that these are off-limb measurements and that they do not take into account the plume area projected on the solar disk.

The contribution of polar plumes to the fast solar wind arising from the polar coronal holes has been a subject of debate and controversy. In general, plumes are thought to harbor smaller outflow speeds than interplume regions (e.g., Habbal 1992; Wang 1994; Hassler et al. 1999). Thus, polar plumes observed above the solar limb seem to be nearly in hydrostatic equilibrium and show small or no line shifts, suggesting that the bulk of the acceleration of the solar wind takes place at greater heights (see Del Zanna et al. 1997; Kohl et al. 1997; Wilhelm et al. 2000; Teriaca et al. 2003). Doppler dimming techniques applied to *SOHO* UVCS (Kohl et al. 1995) observations of the O VI lines have shown outflows in interplume dark lanes ranging from 100 to 150 km s^{-1} at 1.7 $R_\odot$ from Sun center and lower speeds in bright plumes (0–65 km s^{-1}; see Giordano et al. 2000). However, Gabriel et al. (2003) used the Doppler dimming technique applied to *SOHO* SUMER data and found the intensity ratio of the O VI doublet to be smaller in plumes than in interplumes. They concluded that outflow speeds of the solar wind are greater in plumes than in interplumes. Unfortunately, they did not analyze line profiles, in particular the line widths, on which the Doppler dimming effect depends.

EUV coronal emissions in spectral lines that are formed within narrow temperature ranges are excellent temperature diagnostics for different coronal structures. *SOHO* EIT (Delaboudinière et al.

[1] National Solar Observatory (NSO), Tucson, AZ.
[2] Max-Planck-Institut für Sonnensystemforschung, Katlenburg-Lindau, Germany.

1995) images (Fe XII λ195 that forms at $\sim$1.6 MK and Fe IX/X 171 at $\sim$1.0 MK) reveal that plumes are cooler than the background corona (DeForest et al. 1997; Young et al. 1999). Spectral analysis has also shown that UV lines are narrower in plumes than in interplume regions (e.g., O VI λ1032 line widths are 10%–15% lower; Hassler et al. 1997). This suggests that the plume material is relatively cooler than or has less turbulence than dark lane plasma (interplume regions). Wilhelm et al. (1998) used intensity ratios of temperature-sensitive lines for accurate measurements of temperatures in the low corona. They found evidence for an increasing temperature with height in the background corona, but no rise of temperature in plumes (see also Young et al. 1999).

The geometry of plumes is an important key to understanding their contribution to the fast solar wind. The high-speed solar wind at even moderate solar latitudes is thought to originate within coronal holes at high latitudes and to be affected by superradial expansion of the coronal hole magnetic field (Zirker 1977). From white-light observations, plumes are also thought to expand superradially with altitude (Ahmad & Withbroe 1977; Munro & Jackson 1977; Fisher & Guhathakurta 1995). DeForest et al. (1997) found that plumes expand highly superradially (with a half-cone angle of 45°) in their lowest 20–30 Mm, and more slowly above. DeForest et al. (2001a) also found that below $\sim$5 $R_\odot$ plumes expand superradially at the same rate as the background coronal hole. However, Woo & Habbal (1999) and Woo et al. (1999) have claimed to observe radial, rather than superradial, expansion of plumes in the coronal holes. Speculation on interaction between plume and interplume material has been reported, in particular at high altitudes in the corona.

Saito & Tanaka (1957a, 1957b) were the first to associate plumes with magnetic flux concentrations (faculae) in the polar regions. Polar plumes arise from footpoints 2–4 Mm ($\approx$4″) wide and expand rapidly with height (see DeForest et al. 1997). A simulation has shown that a typical plume width at the base of the corona is 20–28 Mm (K. Wilhelm 2006, private communication). Several authors (e.g., Harvey 1965; Newkirk & Harvey 1968; Lindblom 1990; Allen 1994) have suggested that polar plumes arise mainly from unipolar magnetic structures coinciding with the supergranular network boundaries. However, DeForest et al. (1997) have shown that not all of the flux concentrations give rise to polar plumes. Other authors suggest that unipolar magnetic flux concentrations reconnect with ephemeral emergent flux having opposite polarity (e.g., Saito 1965; Wang 1994, 1998; Wang & Sheeley 1995). This is supported by the high temperatures observed at the plume footpoints, producing high-pressure plasma from the dipole that can escape along open field lines. DeForest et al. (2001a) found that polar plumes are of episodic nature: "polar plumes are both transient and persistent: they are recurring structures that brighten for only 1 day but reappear at approximately the same location for up to 2–3 weeks." They speculate that this behavior is the result of multiple magnetic reconnections of the unipolar flux concentrations at the network boundaries encountering multiple ephemeral dipoles and driven by supergranular motion.

We consider model plumes having different outflow speeds and turbulence and calculate the line profile shape of the plume plasma. We use the observed profile shapes of the O VI lines as primary criteria to select the appropriate height variation of those quantities. We then refine them to reproduce the other measured quantities, i.e., line widths, total intensities, and intensity ratios. In the following sections, we study the effect of polar plume locations along the line of sight (LOS) on the line profiles and intensities of the O VI doublet and Lyα. The comparison with the observed quantities deduced from *SOHO* UVCS spectra allows us to constrain the dynamic properties of the plasma inside plumes. In § 2, we present a summary of plume spectroscopic observations by *SOHO* UVCS and highlight the spectral properties of O VI λ1032. A polar plume model is described in § 3, and the results from this model are presented and discussed in §§ 4–7. Conclusions and prospects are found in § 8. A preliminary version of some of the results has been reported by Raouafi et al. (2006).

2. SUMMARY OF UVCS PLUME OBSERVATIONS

The Ultraviolet Coronagraph Spectrometer (UVCS; Kohl et al. 1995) has provided important spectral information on coronal lines in polar holes. The main spectral lines recorded by UVCS are Lyα, the O VI doublet at 103 nm, and the Mg X doublet centered at around 61 nm (in the order of decreasing emission).

Spectral analysis of UVCS data has shown that H I Lyα has, to a good approximation, a Gaussian shape at all heights accessible to this instrument. Kohl et al. (1999) pointed out small deviations from Gaussians at the profile peaks, allowing for two line components resulting from the contributions of different plasma media with different properties along the LOS. Giordano et al. (1997) have also shown that Lyα profiles are narrower when ray paths intersect high-density structures (plumes) than otherwise (interplumes).

The change with height of the O VI line profiles is more complex than for Lyα. While at low altitudes (say below $\sim$1.35 $R_\odot$) the observed profiles are relatively Gaussian shaped, with small deviations in the wings and peaks, more pronounced deviations of the observed profiles from a single Gaussian are clearly seen in the observations at higher altitudes up to about 2.0 $R_\odot$. At this height, the O VI profiles are well represented by two Gaussian components: a narrow and a broad one. The latter appears to be associated with regions of low density (interplume regions), while the narrow component shows a clear association with the denser regions along the LOS (higher emission regions, e.g., polar plumes). The spectral behavior of the two components as a function of height above the limb is quite different. The width of the broad component increases dramatically with height, while that of the narrow one remains almost constant (see Kohl et al. 1997, 1999). Mg X lines have a narrow component at $r = 1.34$ $R_\odot$, accounting for only a small fraction of the observed spectral radiance. For higher altitudes, the observations are not good enough to distinguish whether or not a narrow coronal component exists. Kohl et al. (1999) have also shown that the $V_{1/e}$ values for the narrow components of O VI and Mg X are smaller than those for H I λ1216 at the same heights, and the narrow Mg X value is smaller than that of O VI.

At the solar activity minimum, the polar coronal holes are well developed and bordering streamers appear not to reach the UVCS observation altitudes, making it very likely that narrow components are contributions of fine structures inside the polar coronal hole. Polar plumes are the most prominent features at the heights at which UVCS observes, which makes them the main source of the narrow component observed in the spectral lines.

Figures 1 and 2 display spectral profiles of O VI λ1032 recorded directly above the pole on 1997 September 19–23 and 1996 June 3, respectively, using the $\approx$40′ long UVCS slit. EIT images and Kitt Peak Vacuum Telescope magnetograms clearly show the presence of polar plumes against the solar disk and magnetic concentrations with footpoints at 10°–15° (Fig. 1) and $\approx$20° (Fig. 2) away from the north pole. The profiles in the first figure are formed of two distinct components (narrow and broad). Two Gaussians are needed to give satisfactory fits to the profiles at $r = 1.75$ $R_\odot$ and partly around $r = 2.0$ $R_\odot$ as well, although with a small contribution of the narrow component. However, the profiles in the second figure are very close to a Gaussian in shape, although they show a small degree of asymmetry. Thus, the spectral profiles depend

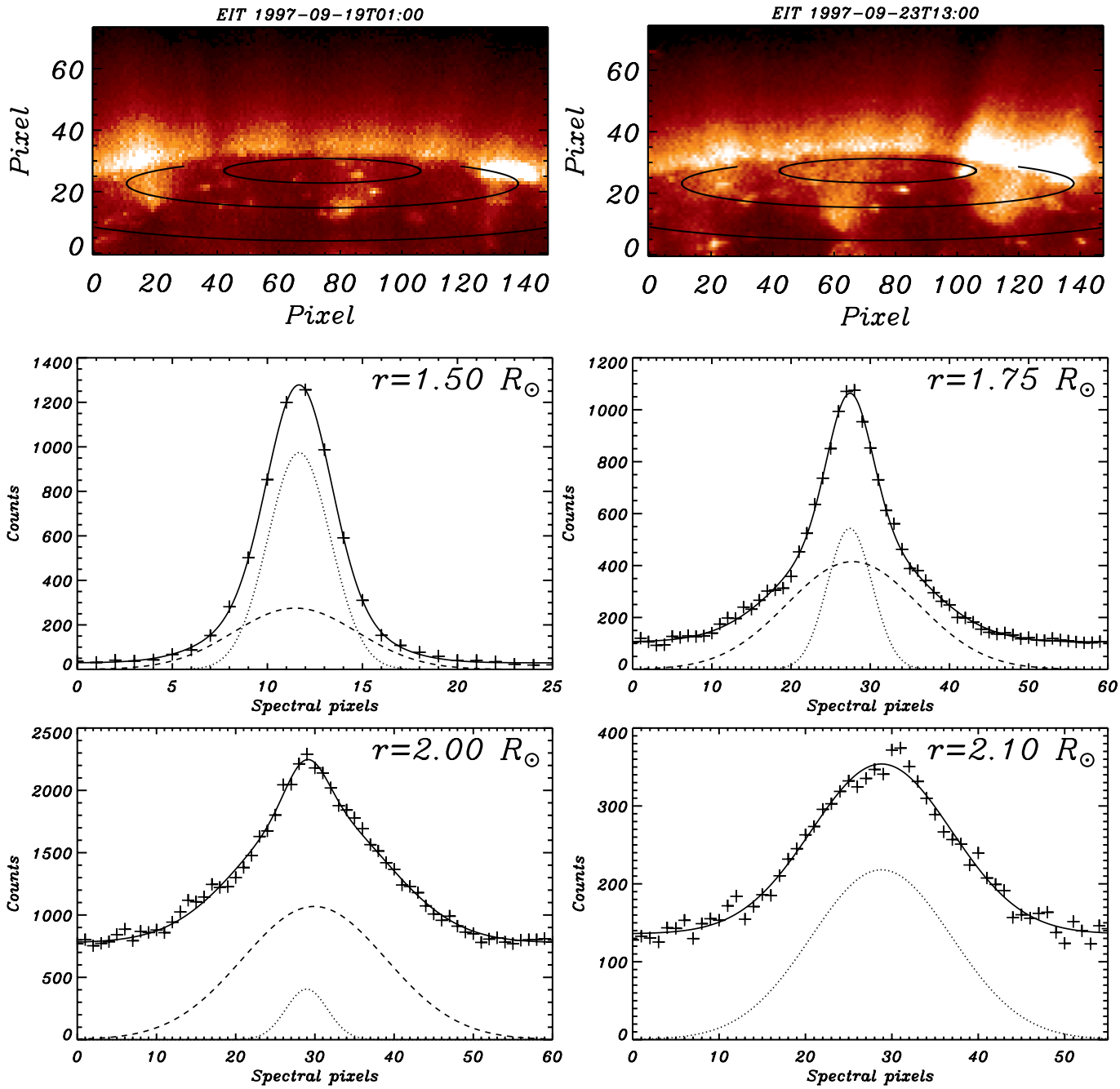

FIG. 1.—*Top*: EIT 171 Å images of 1997 September 19 and 23, respectively. Polar plumes with strong emissions are present more than 10° away from the pole on both days (latitude marked every 5°). *Middle and bottom*: O VI λ1032 line profiles (*pluses*) recorded by UVCS over the same period of time. The profiles are better fit by two Gaussians (*solid curves*), except for the bottom right panel, in which a one-Gaussian fit is equally good. The narrow and wide fit components are represented by dotted and dashed lines, respectively. Counts in the different panels are not normalized to exposure times.

relatively strongly on the distance of the plume footpoints to the pole and also on to the brightness of the plume. In other words, they depend on where the plume crosses the LOS at a given altitude. This difference in the profile shapes is a valuable tool for studying plasma dynamic in these coronal fine structures.

The characteristics of the plumes' spectral contribution (narrow component) to O VI lines, as observed by UVCS, are summarized as follows:

1. Dominates the profiles below $\sim$2.0 $R_\odot$ and decreases above.
2. Not seen in the profiles beyond $\sim$2.5 $R_\odot$. Only the broad component remains above this altitude. Note that the noise level in the profiles increases with height, which might screen small contributions from fine coronal structures along the LOS.
3. Mostly located at the center of the broad component, which is close to the rest wavelength of the spectral lines. Thus, no significant Doppler shifts are observed for the narrow component.
4. The width of narrow component hardly changes as a function of height in the range in which this latter is observed (see Kohl et al. 1997).

3. A MODEL OF POLAR PLUMES

In order to study the influence of polar plumes on the LOS-integrated profiles of O VI and H I, we consider a number of plumes

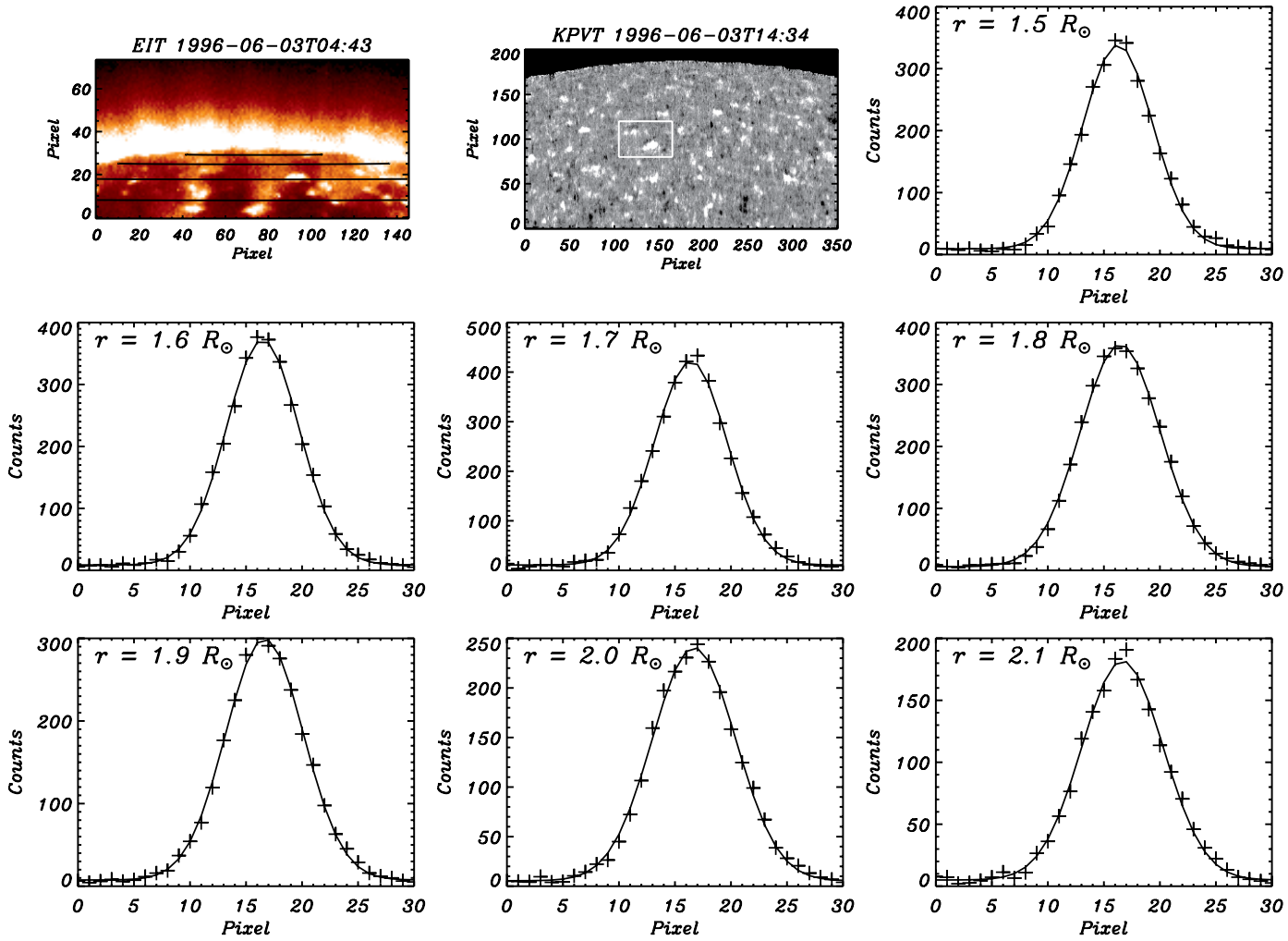

FIG. 2.—EIT 171 Å image (*top left*) and Kitt Peak vacuum telescope magnetogram (*top middle*) of the north solar pole on 1996 June 3. Latitude lines indicate 5° increments. Polar plumes with footpoints about 20° away from the pole are clearly visible in the EIT image. The footpoint of the plumes around pixels (45, 10) in the top left panel lies in the white box in the magnetogram. The other panels display the line profile of O VI λ1032 recorded by UVCS on the same date at different heights (*pluses*). The profiles are slightly asymmetric, although they are fit relatively well by a single Gaussian (*solid curves*).

aligned along the LOS, with footpoints placed at different angular locations in the polar coronal hole (see Fig. 3). The importance of the angular locations of the plume footpoints is enhanced because of the superradial expansion of the magnetic field. The footpoint location determines the LOS outflow speed of the plume plasma at the location where the plume crosses the LOS. Based on the work of DeForest et al. (2001a) and others, we assume that plumes expand superradially at the same rate as the surrounding background corona (interplumes), according to the global magnetic model by Banaszkiewicz et al. (1998). The electron density is considered to be greater in plumes than in interplumes, following Wilhelm et al. (1998) and Wilhelm (2006). The density contrast is largest just above the solar surface and decreases gently with height, such that it disappears above $\approx 7\,R_\odot$ (see set in Fig. 4). The interplume electron density stratification is obtained from *SOHO* data (SUMER, UVCS, and LASCO [Brueckner et al. 1995]; see Doyle et al. 1999a, 1999b; Fig. 4, *solid line*). The density profile of plumes (Fig. 4, *dashed line*) is obtained by considering a higher density at the footpoints at the solar surface ($\approx 9 \times 10^8$ cm^{-3}; see Del Zanna et al. 1997; Young et al. 1999) and a lower temperature inside plumes ($\approx 10^6$ K) than in interplumes (1.5×10^8 cm^{-3} and 1.2×10^6 K, respectively, for the model by Doyle et al. 1999a, 1999b). The variation of both densities as a function of height is given by equation (1) in Doyle et al. (1999a, 1999b).

We assume that the considered coronal species have simple Maxwellian velocity distributions inside both plume and interplume regions, but with different velocity turbulence values, $\alpha_s(r)$, which are functions only of height in both structures. The plume outflow speed, $V_{\rm pp}$, is assumed to be proportional to the

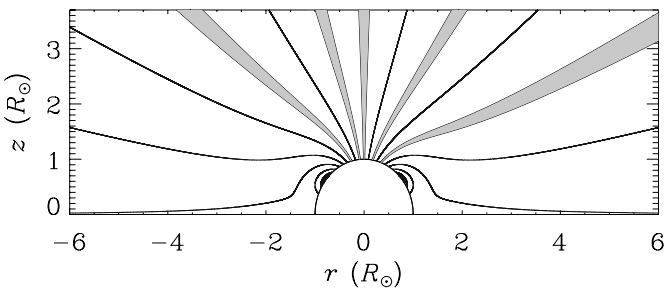

FIG. 3.—Spatial distribution of the polar plumes used for the calculations of the coronal line profiles in the plane of the LOS. The plume footpoints are 18 Mm wide and are centered at angular positions relative to the pole from left to right: −15°, −5°, 0°, 10°, and 18°, respectively. The magnetic field is assumed to expand similarly in both plume and interplume regions. No plumes are placed farther than 20°, since these plumes do not reach large apparent heights above the pole due to the rapid expansion of the magnetic field. However, their presence may affect profiles at low altitude (below $\approx 2.5\,R_\odot$).

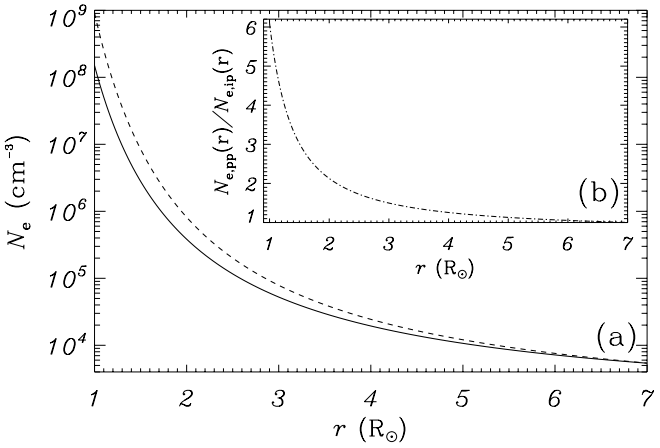

FIG. 4.—(*a*) Electron density stratifications inside plumes (*dashed line*) and interplumes (*solid line*). The interplume density is that obtained from *SOHO* (SUMER, UVCS, and LASCO) data (see Doyle et al. 1999a, 1999b). The plume density stratification is obtained by imposing a greater density at the solar surface (see text for reference) and lower temperature in plumes relative to the surrounding ambient corona. (*b*) Plume-interplume density ratio as function of height.

solar wind speed in interplume regions, V_{ip}, and the proportionality coefficient is assumed to depend only on the radial distance to Sun center: $V_{pp}(r) = g(r) \times V_{ip}(r)$, where $V_{ip}(r)$ is obtained through the mass-flux conservation equation. Because of the lack of conclusive observational results concerning $g(r)$ and $\alpha_{s,\,pp}(r)$, we consider height profiles for each.

Two cases are considered for the plume velocity turbulence: $\alpha_{s,\,pp}(r) =$ constant ($\approx$50 km s^{-1} for the O VI lines following observational values from Kohl et al. 1997, 1999) and a height-dependent turbulent velocity $\alpha_{s,\,pp}(r) = f(r)$. The value of 50 km s^{-1} is approximately the observed width of the narrow component, as measured at 1.34 $R_\odot$ (see Fig. 3 of Kohl et al. 1999). In the latter case, a low turbulence value is prescribed at low altitudes, which increases to reach the interplume value above $r \approx 6.0\ R_\odot$. Three cases are considered for $g(r)$: constant, linear, and nonlinear.

4. TEST CASES OF THE TURBULENCE AND OUTFLOW EVOLUTION INSIDE POLAR PLUMES

The data presented in Figures 1 and 2 correspond to plumes based between $\approx 10^\circ$–20° from the pole. In order to compare our simulations with these observed profiles, we limit ourselves in this section to the very left plume in Figure 3, which has its footpoint centered at 15° from the pole. This plume lies between the examples shown in Figures 1 and 2.

In this section, we consider the four test cases (§§ 4.1–4.4) presented in Table 1. Note that we have also computed the lines for the remaining combinations of $\alpha_{s,\,pp}$ and V_{pp}, but nothing new was learned from them.

For the interplume regions, the plasma properties are similar to those found by Raouafi & Solanki (2004, 2006). The theoretical formalism used here for the line profile computations is discussed by Raouafi & Solanki (2004) and references therein. In the present section, we limit ourselves to discussing the profiles of the O VI λ1032 line. O VI λ1037 is also computed and is found to behave similarly to the λ1032 line. Lyα profiles are also computed, but this line is less sensitive to the behavior of α_s and V, and its shape does not change as much as that of O VI λ1032. Thus, in contrast to the O VI lines, the Lyα profile is close to a Gaussian for most plume parameters and at most heights.

TABLE 1

TEST CASES OF THE TURBULENCE AND OUTFLOW HEIGHT DEPENDENCE IN POLAR CORONAL PLUMES

Case	$\alpha_{s,\,pp}(r)$	$V_{pp}(r)$
1	C	$C' V_{ip}(r)$
2	C	$\begin{cases} (ar+b)V_{ip}(r) & \text{if } V_{pp} < V_{ip}, \\ V_{ip}(r) & \text{otherwise} \end{cases}$
3	$f(r)$	$\begin{cases} (ar+b)V_{ip}(r) & \text{if } V_{pp} < V_{ip}, \\ V_{ip}(r) & \text{otherwise} \end{cases}$
4	$f(r)$	$g(r)\ V_{ip}(r)$

NOTE.—C, C', a, and b are constants.

4.1. *Case 1: Constant Velocity Turbulence and Proportional Flow*

In the first step, we consider a plasma outflow speed inside plumes that is equal to a constant fraction of that in the interplume regions. Plume speeds that are smaller and greater than interplume values are considered [$V_{pp}(r)/V_{ip}(r) = 0.25$, 0.5, 1.0, and 1.5]; $\alpha_{s,\,pp}$ is height independent and equal to 50 km s^{-1}.

Figure 5 displays the profiles of the LOS-integrated O VI λ1032 line at 1.7 and 3.0 $R_\odot$ for different V_{pp}/V_{ip} values. For small V_{pp}/V_{ip}, the plume contribution (narrow component) dominates the profiles at low altitudes, showing some resemblance to the observed profiles (see solid lines in Figs. 5*a* and 5*b*). However, at high altitudes the narrow component is still clearly present with a strength well above the typical noise level present in the observed profiles. For greater values of V_{pp}/V_{ip} (Figs. 5*c* and 5*d*), the plume contribution is Doppler shifted away from the line peak already at low altitudes (due to the location of the considered plume relatively far from the pole). This produces strongly asymmetric profiles, unlike the observed ones. Also, the plume contribution is still significant at high altitudes. The present case ($\alpha_{s,\,pp}$ = constant and V_{pp}/V_{ip} = constant) does not reproduce the overall observed profiles. Consequently, it does not reflect the plasma conditions and mechanisms and the fact that it is taking place in polar plumes.

Nonetheless, the computations suggest that outflow speeds in plumes are likely to be much smaller ($V_{pp}/V_{ip} < 0.25$) than interplume values at low altitudes. This avoids large contributions from plumes far from the central wavelength of the observed lines irrespective of their footpoint location. Plume outflow speeds close to or greater than the interplume values at low altitudes will be excluded from the rest of the analysis.

4.2. *Case 2: Constant Velocity Turbulence and Linear-Height-Proportional Flow*

In this section, we keep a height-independent velocity turbulence inside plumes ($\alpha_{s,\,pp} = 50$ km s^{-1}). However, the plume-interplume outflow speed ratio is now allowed to vary linearly with height, such that

$$V_{pp}(r) = \begin{cases} (ar+b)V_{ip}(r) & \text{if } V_{pp}(r) < V_{ip}(r), \\ V_{ip}(r) & \text{otherwise}, \end{cases} \quad (1)$$

where a and b are constants chosen such that $(ar + b)$ is zero or very close to zero at the solar surface and increases toward unity at high altitudes, roughly above 6 $R_\odot$. A possible mechanism for such an acceleration of the plume plasma could be interaction with the surrounding background medium having higher outflow speeds.

We consider the three height profiles of $V_{pp}(r)/V_{ip}(r)$ that are given in Figure 6*a*. LOS-integrated profiles computed along rays

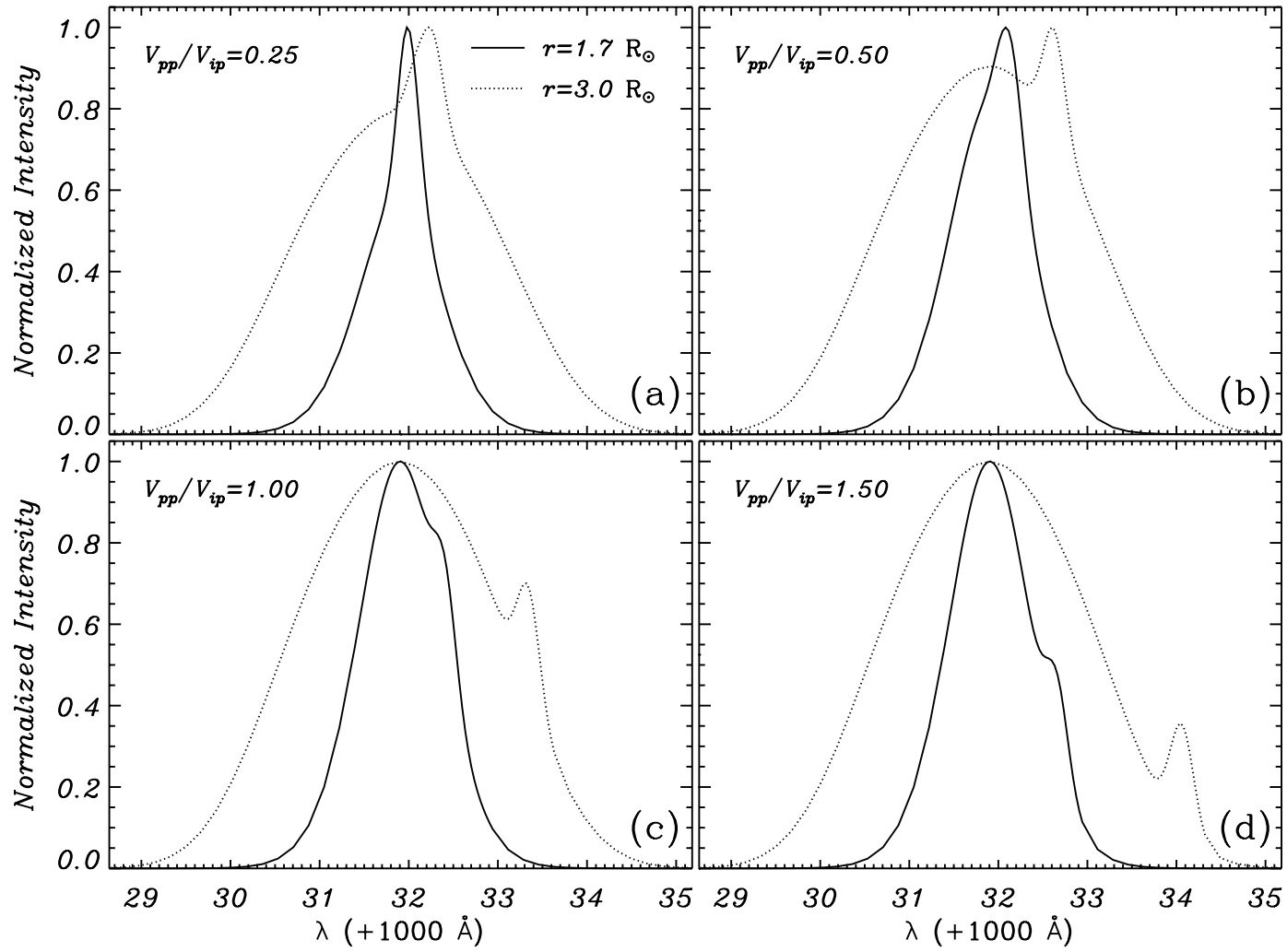

FIG. 5.—Case 1: LOS-integrated model profiles of the O VI λ1032 line at 1.7 $R_\odot$ (*solid lines*) and 3.0 $R_\odot$ (*dotted lines*) in the presence of the very left polar plume in Fig. 3. The plume velocity turbulence is assumed to be constant and the outflow speed is equal to a height-independent fraction of the interplume outflow speed, as noted in the different panels.

reaching 2.0 and 3.0 $R_\odot$ from disk center are plotted in Figures 6*b* and 6*c*. The obtained profiles are to some extent similar to those in Figure 5 for $V_{\rm pp}(r)/V_{\rm ip}(r) =$ constant. Although the profiles at low altitudes now all have the narrow component nearly centered at the broad component, which is close to the observations, those obtained at high altitudes have the same significant narrow contributions shifted to the wings of the profile. Such a signal is not observed in the corona.

4.3. *Case 3: Nonlinear-Height-Dependent Velocity Turbulence and Linear-Height-Proportional Flow*

The plume outflow speed is that of case 2, while the velocity turbulence of the plume plasma is assigned a height-dependent function. A variation in the velocity turbulence appears natural if cool plume and hot interplume material interacts. Due to the lack of observational results concerning the variation of both parameters, we assume, for simplicity, similar profiles for the turbulence inside plumes and interplumes $\alpha_{s,\,\rm ip}(r)$. Thus, $\alpha_{s,\,\rm pp}(r)$ has the following functional form (see Raouafi & Solanki 2004, 2006):

$$\alpha_{s,\,\rm pp}(r) = \kappa \arctan(r^{\eta} + \mu) + \delta, \qquad (2)$$

where κ (=205/π), η (=1.5), μ (=4.5), and δ (=130) are adjustable parameters whose values have been selected in order to get as close as possible to the observations. Since there is observational evidence for cooler plasma in plumes than in interplumes, we assume that $\alpha_{s,\,\rm pp}(r)$ is smaller than $\alpha_{s,\,\rm ip}(r)$ at low altitudes and converges gently toward the large values of $\alpha_{s,\,\rm ip}(r > 6\ R_\odot)$ (see Fig. 7*a*). This guarantees the presence of a narrow component at low heights and progressively broader plume profiles as we move further above the solar limb.

Figures 7*b*–7*h* display the O VI λ1032 line profiles obtained for lines of sight ranging from 1.5 to 3.5 $R_\odot$ above the pole for the plume outflow speed profiles shown in Figure 6*a*. At altitudes below $\approx$1.5 $R_\odot$, the contribution of polar plumes to the line profile is narrower than that of interplumes, and is approximately centered at the rest wavelength of the line. This results in approximately Gaussian-shaped line profiles that are slightly narrower than those obtained without polar plumes (see Fig. 7*b*). For 1.5 $R_\odot \le r \le$ 2.5 $R_\odot$, a profile that can be well represented by two Gaussians and that resembles the observed profiles is obtained (Figs. 7*c*–7*f*). The broad component is due to interplume material, the narrow component to plumes. Due to the low plume outflow speeds at these altitudes, the Doppler shift of the narrow component is low.

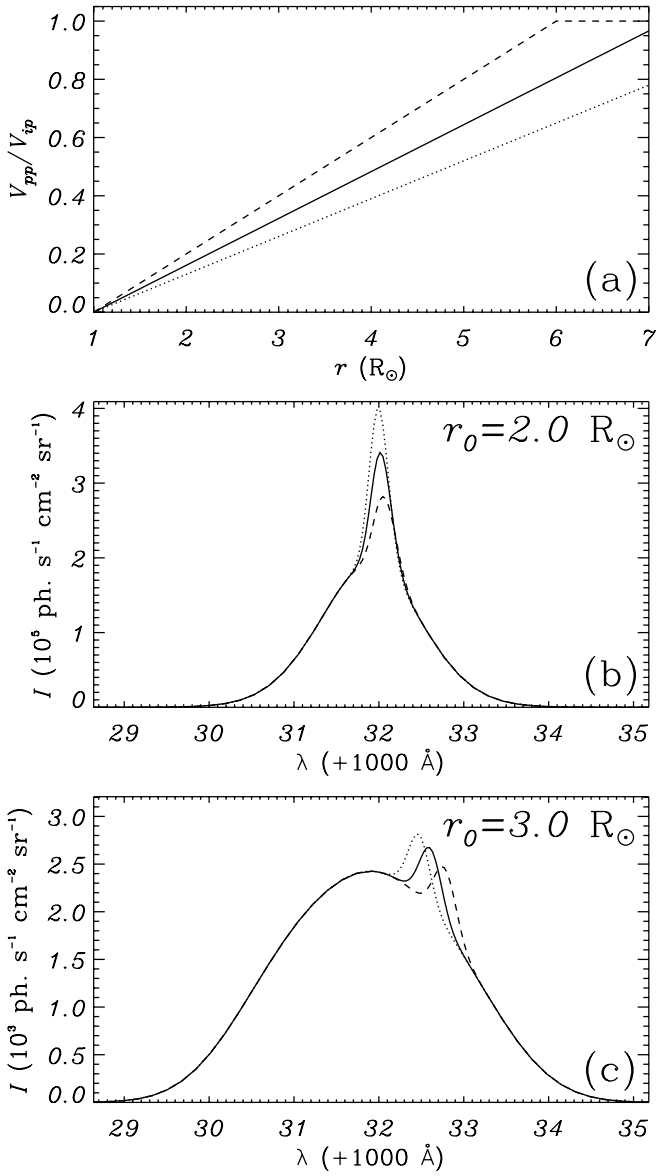

FIG. 6.—Case 2: O VI λ1032 line profiles for a wind speed in plumes equal to a linear-height-dependent fraction of the interplume outflow speed and a constant velocity turbulence in plumes. (*a*) Chosen flow speed height profiles, (*b*) resulting line profiles at 2.0 $R_\odot$, and (*c*) at 3.0 $R_\odot$ from Sun center.

Above $\approx$2.5 $R_\odot$, the increase in the plume velocity turbulence results in increasingly broader plume contributions, so that the line profile (see Figs. 7*g* and 7*h*) takes on the approximate shape of a single Gaussian for the dashed velocity profile in Figure 6*a* (*dotted lines*). For the other velocity models, the plume component is narrower, particularly, for the dotted plume velocity model, so that one can still distinguish two line components at high altitudes. Hence, high plume outflow speeds at $r \geq 2.5$ $R_\odot$ that are closer to interplume values fit the observations better than smaller ones.

The present case is in better agreement with the observation than cases 1 and 2, although the agreement is not perfect, both at very low and very high altitudes. For example, at low altitudes the plume contribution does not dominate the LOS-integrated profiles. Probably, the plume outflow speed at these altitudes is still high enough to dim the radiative plume component (shifted from resonance due to the small velocity turbulence). Improvement can be obtained by considering a nonlinear height-dependent $V_{\rm pp}(r)/V_{\rm ip}(r)$, allowing for lower and higher plume speeds at low and high altitudes, respectively. This is the aim of case 4.

4.4. *Case 4: Nonlinear-Height-Dependent Velocity Turbulence and Nonlinear-Height-Proportional Flow: Case Best Reproducing Observations*

The velocity turbulence in plumes $\alpha_{s,\,\rm pp}(r)$ is again described by equation (2) and is illustrated by the dash-double-dotted curve in Figure 7*a*. The plume outflow speed is now considered to be related in a nonlinear way to the interplume speed:

$$V_{\rm pp}(r) = g(r)\, V_{\rm ip}(r), \qquad (3)$$

where $g(r)$ is illustrated by the solid line in Figure 8*a*. The plume-interplume solar wind speed ratio is less than 10% below $\approx$2.0 $R_\odot$ from Sun center, and increases abruptly to more than 75% by about 3.0 $R_\odot$, then converges gently toward unity. This profile allows more contribution from the plume radiative component at $r \leq 2.0$ $R_\odot$ and favors broader plume profiles at $r \geq 3.0$ $R_\odot$.

The LOS-integrated O VI λ1032 line profiles are displayed in Figures 8*b*–8*h*, together with the plume (*dotted lines*) and interplume (*dashed lines*) contributions. The plume contribution is now, as expected, more significant at low altitudes, in particular below $\approx$1.7 $R_\odot$, and dominates the profile below $\approx$1.4 $R_\odot$ (see Fig. 8*b*).

The change in the plume contribution is due partly to combined effects of the electron density decrease, but mostly to the variation of the outflow speed and turbulence of the plasma inside plumes. The calculated profiles are close to a Gaussian shape at $r \leq 1.3$ $R_\odot$ and display increasingly a bi-Gaussian shape above this altitude up to $r \geq 2.0$ $R_\odot$ (Figs. 8*c* and 8*d*). Above $\approx$1.3 $R_\odot$, the obtained profiles cannot be represented by one Gaussian, and the two components (narrow and broad) can be distinguished even without fitting. The width of the plume component increases relatively rapidly above $\approx$2.0 $R_\odot$, and so does its Doppler shift. This sudden change in the profile of the plume contribution allows the two (broad and narrow) components to merge completely above $\approx$2.3 $R_\odot$. The resemblance of the computed profiles to the observed ones is now uniformly good (compare profiles in Figs. 1 and 8). Note that greater gas densities in plumes above 7.0 $R_\odot$ than the one considered here allow for a greater contribution from plumes, which results in broader LOS-integrated profiles at high altitudes that are even closer to the observed ones. Any remaining small differences between computed and observed profiles could also reflect the footpoint location of the modeled plume, or the possible presence of multiple plumes along the LOS in the observations.

Case 4 best reproduces the observed profile shapes. We expect this model to be the closest to the plasma conditions in the polar plumes. In other words, the plume material remains cooler and much slower than the interplume plasma up to $\approx$2.0 $R_\odot$ from Sun center, where a rapid increase in both outflow speed and effective temperature takes place, leading to plume dynamic properties converging toward those of interplume region within the next solar radius. The rapid change in plume plasma properties is likely to be due to interaction between the cool and slow plume and hot and fast interplume materials, although some authors speculated that this interaction takes place much higher in the solar corona (see § 1). In the next sections, we will consider this case only for an extensive study of the profiles and total intensities of the different spectral lines considered here. The contribution

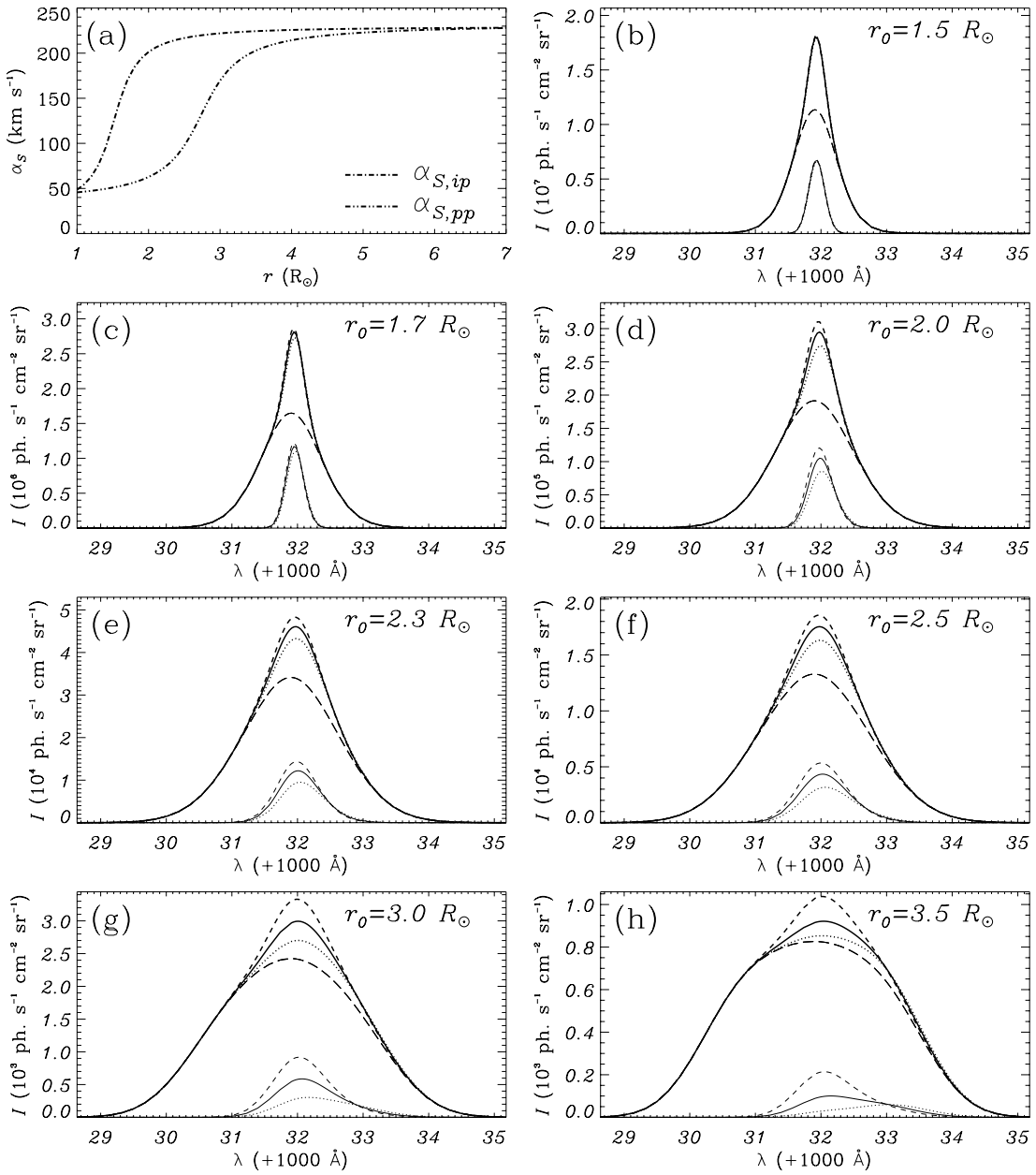

FIG. 7.—Case 3: (*a*) $\alpha_{s,\mathrm{pp}}(r)$ and $\alpha_{s,\mathrm{ip}}(r)$ as a function of height used for the computation of the profiles in all but the first panel. (*b–h*) O VI λ1032 LOS-integrated profiles corresponding to the three plume velocity models shown in Fig. 6 are given with the same line style as in that figure. Plume (*smaller, narrower profiles at the bottom of each panel*) and interplume (*long dashed curves*) contributions are also plotted.

of polar plumes located very close to or on the pole will also be discussed.

5. O VI DOUBLET

Figure 9 displays the height dependence above the pole of the O VI λ1032 line width (Fig. 9*a*) and total intensity (Fig. 9*b*), as well as of the intensity ratio of the O VI doublet (Figs. 9*c* and 9*d*) from slightly above the solar limb to 3.5 $R_\odot$ from Sun center. The profiles underlying this figure were computed according to case 4 (§ 4.4). They were fit with two Gaussians below 2.0 $R_\odot$ and with one Gaussian above. The widths of the broad and narrow components and of the single-Gaussian fit are represented by different symbols. Also plotted are values obtained from UVCS spectra, together with their corresponding error bars according to Kohl et al. (1997) and Cranmer et al. (1999). The narrow component widths hardly change with height up to 2.0 $R_\odot$ and fit the measured values relatively well. The widths of the broad component, however, change rapidly with height, leading to a non-Gaussian shape of the composite profiles. Higher up, the obtained line widths are comparable to those obtained by Raouafi & Solanki (2006; Fig. 8), although they lie somewhat close to the measurements, in particular around 2.0 $R_\odot$.

Total intensities are also comparable to those computed by Raouafi & Solanki (2006), although the intensities below 2.0 $R_\odot$ fit the observed values for the O VI λ1032 line better. The change in total intensities can be more clearly seen in the intensity ratio of the O VI doublet. Above 1.5 $R_\odot$, the ratios obtained from the composite profiles (*filled circles*) are improved compared to the case without plumes (*open circles*), in particular at low altitudes. All the computed ratios now lie inside the error bars of UVCS

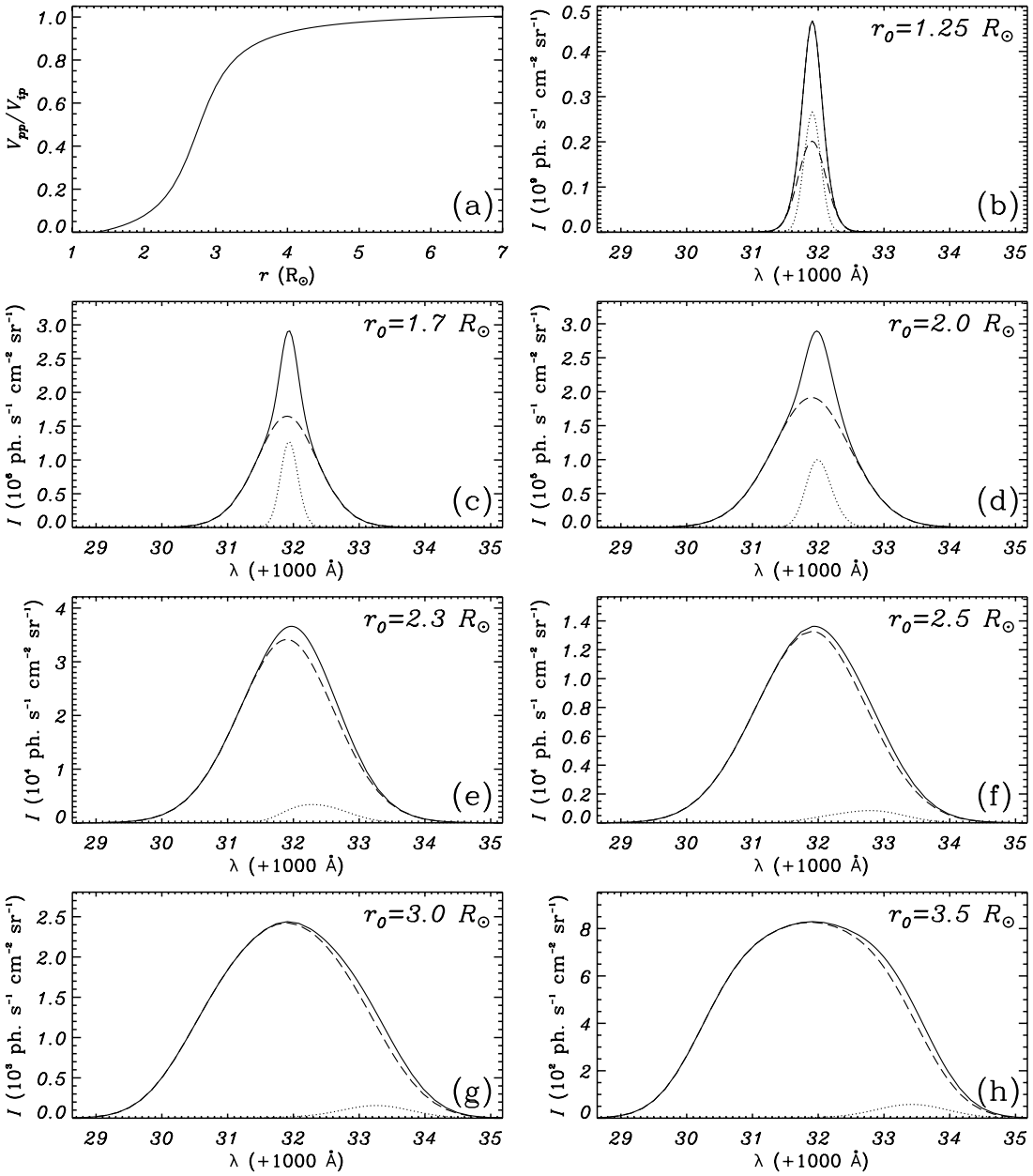

FIG. 8.—Case 4: (*a*) Same as Fig. 7, but for plume outflow speed equal to a nonlinear height-dependent fraction of interplume speed. (*b*–*h*) Line profiles computed along different rays now show considerable similarity to the observed ones. The contribution of plumes (*dotted lines*) is more significant at low altitudes and is extensively dimmed relative to the interplume contribution (*dashed lines*) at higher altitudes. Line profiles are fit by two Gaussians up to 2.0 $R_\odot$ and by a single Gaussian for greater heights.

measurements. Note that only simple Maxwellian velocity distributions are used, and no anisotropy in the kinetic temperature of the O VI ions is considered. Below 1.5 $R_\odot$, the intensity ratios with plume contribution taken into account are smaller than those without plume contribution (see bottom panels of Fig. 9). In our computations, this is due to the large electron density numbers in plumes compared to interplume densities and is not a solar wind effect as reported by Gabriel et al. (2003, 2005). In addition, we showed previously that plume wind speeds faster than or close to interplume speeds give line profiles different from those observed in the polar coronal holes. Here we demonstrate that the fast solar wind originates mainly from interplume regions and that the plume plasma remains slower and cooler up to approximately 2.0–3.0 $R_\odot$ from Sun center (see Fig. 9).

6. H I Lyα LINE

Figure 10*a* displays the velocity turbulence used for the computation of Lyα (solid line for interplume and dotted line for plume). We assume the same $V_{\mathrm{pp,\,Ly}\alpha}(r)/V_{\mathrm{ip,\,Ly}\alpha}(r)$ variation of the plume velocity turbulence as in the case of the O VI ions: small values at low altitudes and a rapid increase toward interplume values above $\approx$2.0 $R_\odot$. The plume-interplume ratio of the outflow speed of the hydrogen atoms is assumed to be the same as for the O VI ions in the previous section (see Fig. 8*a*). Note that the hydrogen outflow speed in interplume regions is lower than that of O VI ions (see Raouafi & Solanki 2006).

The computed line profiles of Lyα are shown in Figures 10*b*–10*j* (*black solid lines*) together with the plume (*black dash-dotted*

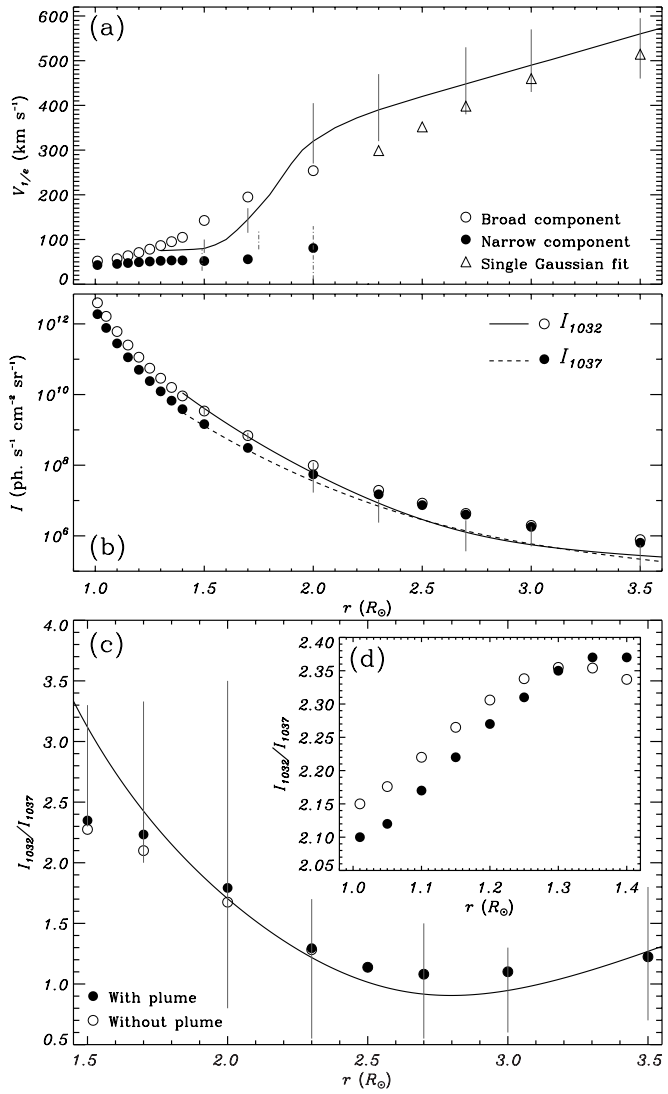

FIG. 9.—*Circles and triangles*: Model (*a*) line width , (*b*) total intensity, and (*c*, *d*) intensity ratio of the O VI doublet vs. *r*. Values obtained from synthetic line profiles following case 4 (profiles plotted in Fig. 8) are shown as filled and open circles and triangles, respectively. The solid and dashed lines are best fits to UVCS observations, and the solid error bars represent the accuracy of the observations (see Cranmer et al. 1999). The dash-dotted vertical bars represent the uncertainty in the observed narrow component widths (see Kohl et al. 1997).

lines) and interplume (*black dotted lines*) contributions for different rays crossing the polar solar axis at different heights. The gray dashed curves are single-Gaussian fits to the computed profiles. The high quality of the fits at all heights demonstrates how close the computed profiles are to a Gaussian shape. However, small deviations from the single-Gaussian shape are noticeable, in particular at low altitudes in the wings and peaks of the profiles. Kohl et al. (1999) observed similar deviations and interpreted them as being due to the contribution of polar plumes. Note that slightly changing (≈10%–20%) the model parameters (i.e., the outflow speed and turbulence of the plasma inside plumes) does not change much the obtained profiles, which remain Gaussian shaped to a good approximation.

The widths of the computed line profiles are displayed in Figure 10*k* as a function of the projected heliocentric distance of the corresponding rays (*filled circles*). The widths obtained without plumes (*open circles*) are also displayed for comparison, together with the best fit to UVCS observations (*solid curve*) and the error bars of the observed values (*vertical lines*; see Cranmer et al. 1999). Line widths obtained in both cases (with and without polar plumes) are within the errors bars of the measured values. However, the widths obtained with plumes taken into account fit the observed values better. By optimizing the number and position of plumes and their properties, an even better match to the observations may be obtained.

Figure 10*l* shows the total intensity of Lyα. The best fit to the observed intensities along with the error bars are also displayed for comparison. At low altitudes, intensities obtained with plumes taken into account are very similar to those without plumes and are slightly greater than the measured ones. However, at higher altitudes intensities obtained with plumes provide an improved fit to the observations. Generally, the presence of plumes along the LOS slightly increases the total intensity due to the density enhancement in plumes.

7. ON THE FOOTPOINT LOCATIONS OF POLAR PLUMES

Figures 11*a*–11*d* shows the LOS-integrated profiles of the O VI λ1032 line with contributions from each of the four right-hand plumes in Figure 3 taken into account separately. The contributions from the two polar plumes based at colatitude -5° and 0° (the narrow component of the line profile) dominate the profiles up to $\approx$2.5 $R_\odot$ and remain clearly visible up to $\approx$3.5 $R_\odot$ (*dotted and solid lines*), which is not the case for the observed profiles. The reason for the continuing visibility of the truly polar plumes up to large altitudes is that the rapid acceleration of the solar wind in the plume hardly affects the plume profile, since it is almost perpendicular to the LOS. The contribution from the plume at 10° is important at low altitudes, but relatively small at high altitudes (*dashed lines*). This suggests that polar plumes preferentially originate more than $\approx 10^\circ$ away from the pole. The contribution from the plume with the footpoint at 18° (*dot-dashed lines*) is very similar to that shown in Figure 2 due to plumes $\approx 20^\circ$ from the solar pole.

Various authors have studied locations of polar plume footpoints within polar regions. They traced plumes arising near the edges of coronal holes, relatively far away from the solar pole (eclipse observations; see Saito 1965). In contrast, we did not find any report on plumes very close to the polar axis. This case may be very rare for unknown physical reasons (for example, bipolar flux may not emerge near the pole).

Polar coronal plumes can be easily identified off-limb in white-light (LASCO, eclipses) and EUV (EIT, *TRACE*) images. On the solar disk, for instance by using EIT images, it is also possible to trace them back to the solar surface, in particular, using images recorded in the wavelength bands containing the hot lines λ171 and λ195, which are regularly recorded by EIT. X-ray images also allow the determination of the locations of plume footpoints, which correspond very often to bright points reflecting the high temperatures there. Once the plume footpoints are identified, it is relatively easy to link them to the underlying magnetic structures using magnetograms. Data recorded daily over several consecutive days, or better still, weeks, help to survey the latitudes of polar plume footpoints. For this purpose, periods of time when the solar axis is tilted toward the observer are more useful, since the observation of a major area of the polar coronal hole including the pole is possible. These times correspond to March and September of each year.

EIT images recorded at solar minimum seem to support this hypothesis. An average of all daily unsigned SOLIS (Synoptic Optical Longterm Investigations of the Sun) high-sensitivity magnetograms recorded in 2005 September (see bottom panel of Fig. 11) show magnetic flux concentrations preferentially between $\approx 70^\circ$ and $\approx 80^\circ$ latitude, although we are not at solar minimum yet. Another reason plumes are more likely to have their footpoints

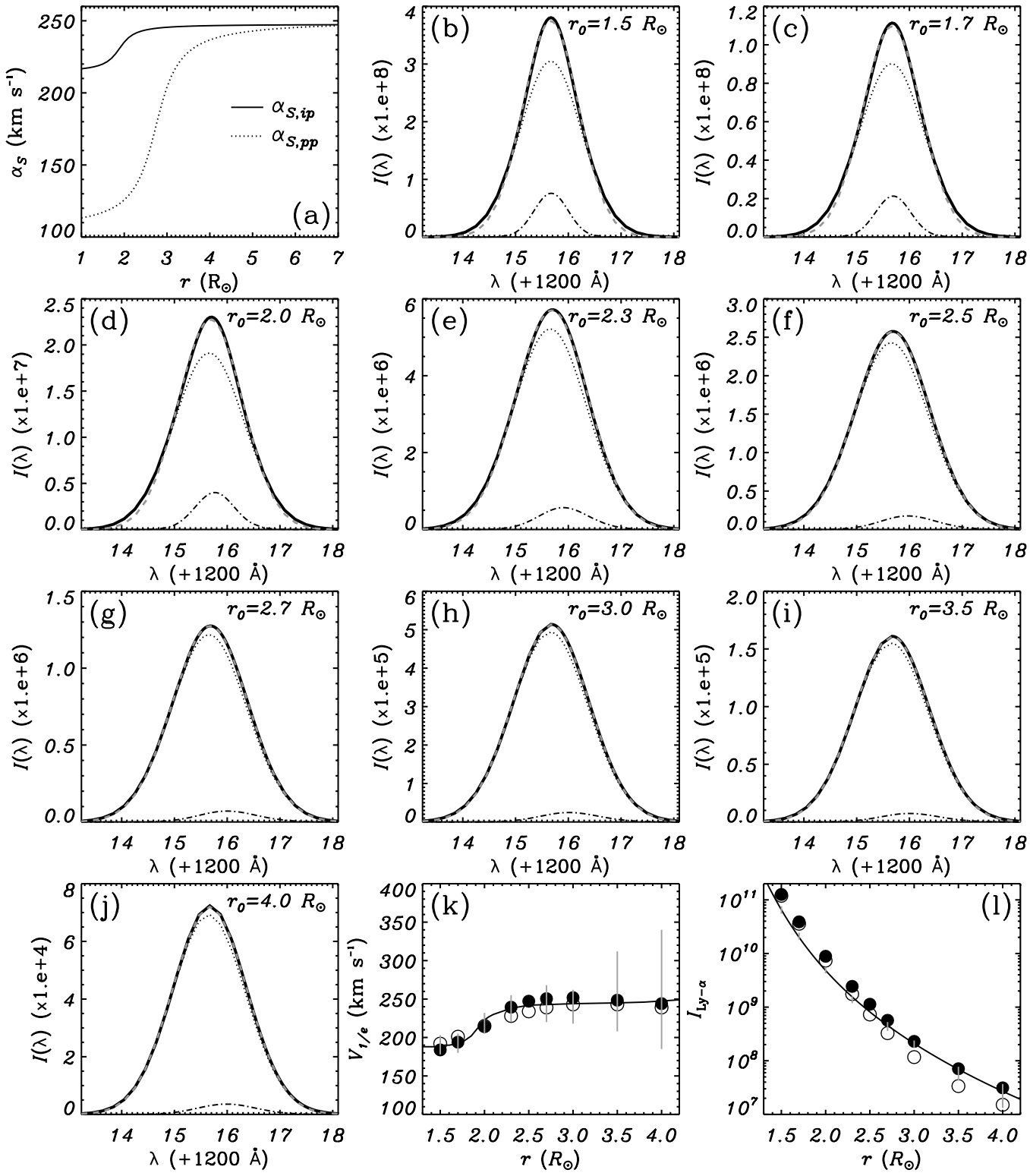

FIG. 10.—(*a*) Velocity turbulence of hydrogen atoms in a plume (*dotted line*) and in interplume (*solid line*) as a function of height. (*b–j*) Computed Lyα profiles: composite profile (*black solid lines*); the plume and the interplume contributions (*black dotted* and *black dash-dotted lines*, respectively); and single-Gaussian fits to the composite profiles (*gray dashed lines*). (*k*) Computed profile widths and (*l*) total intensities of Lyα with (*filled circles*) and without (*open circles*; see Raouafi & Solanki 2006) polar plume crossing the LOS. The solid curves in (*k*) and (*l*) are the best fits to UVCS measured values, together with the error bars of the measurements (see Cranmer et al. 1999).

some degrees away from the pole has to do with the fact that the relative area available for plumes between 70° and 80° is 3 times larger than at latitudes above 80°. However, preliminary analysis of SOLIS magnetograms tends not to support the area argument. This subject will be addressed in detail in a subsequent publication.

8. DISCUSSION

The aim of the present study is to obtain information on the height evolution of the plasma dynamics inside polar plumes. We compared profile shapes of the O VI doublet (λ1032 and λ1037)

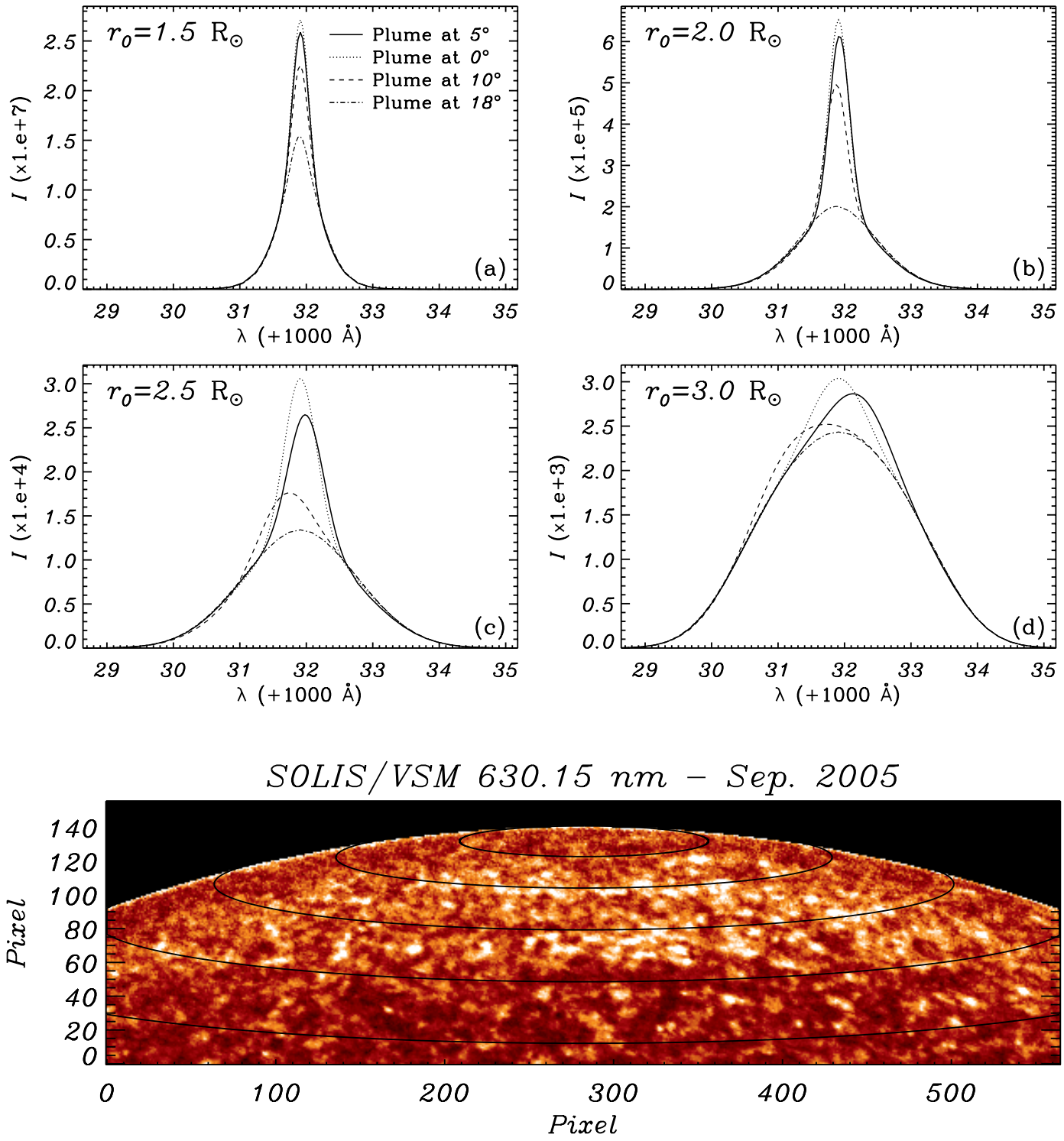

FIG. 11.—(*a*–*d*) Line profiles of the O VI λ1032 line at different altitudes with the individual contributions of the four right-hand plumes in Fig. 3 taken into account separately. The intensity unit is photons s^{-1} cm^{-2} sr^{-1} $Å^{-1}$. Contributions from plumes at or close to the pole are noticeable beyond 2.5 $R_\odot$, which is not the case for the observed profiles. Note the great similarity of the dot-dashed lines (with contribution from the farthest plume to the pole [18°]) with the observed profiles in Fig. 2. *Bottom*: SOLIS magnetograms averaged over 2005 September showing the unsigned flux distribution around the north polar coronal hole. The flux is concentrated preferentially between 70° and 80° latitudes. The solid curves mark latitudes every 5°.

and the H I Lyα spectral lines, observed by *SOHO* UVCS at different altitudes in polar coronal holes, to synthetic profiles that include the contribution of polar plumes placed at different locations along the LOS. Observational constraints on these fine coronal structures (e.g., densities, temperatures, geometry) have been taken into account following different reports in the literature. Since the outflow speed and kinetic temperature evolution with height are not conclusively known, we consider different height profiles for the outflow speed and plasma turbulence inside plumes and study how these choices influence the line profiles of the O VI doublet, which are more sensitive to the detailed dynamic structure along the LOS than H I Lyα.

By comparing the synthetic profiles to the observed ones in the polar coronal holes, we determined plausible height profiles for the outflow speed and plasma turbulence in polar plumes with respect to the surrounding background corona. We find that models with constant (height-independent) velocity turbulence in the plumes show narrow components with a significant contribution to the LOS-integrated profile at all heights, in particular above $\sim 3.0\ R_\odot$, where there is no observational indication of the presence of such a narrow component in the observed profiles. This is independent of whether the plume outflow speed equals a constant or a height-dependent fraction of the interplume outflow speed. Synthetic profiles with shapes very similar to the observed ones are obtained when the plasma turbulence in plumes is height-dependent, with similar variation to that in interplume regions, and converges toward the latter at greater heights. At the same time, the outflow speed is small near the solar surface, but approaches the interplume value at greater heights. The narrow component is found to contribute significantly to the resultant profiles at altitudes below $\sim 2.0\ R_\odot$ and is increasingly dimmed above that altitude. This model suggests that the plume plasma remains much slower and cooler (in the sense that $\alpha_{s,\,\mathrm{pp}} < \alpha_{s,\,\mathrm{ip}}$) than interplume material up to $\approx 2.0\ R_\odot$. Above $\approx 2.0\ R_\odot$ these parameters experience a rapid rise toward interplume values reached by $\approx 3.0\ R_\odot$. The rapid acceleration and increase in the effective temperature of the plasma inside plumes is probably the result of interaction with the faster and hotter interplume material. The entrainment or mixing of material between plumes and interplumes is hindered by the magnetic field. The smaller the magnetic energy density relative to the thermal or the kinetic energy density, the more efficiently entrainment takes place. Now consider the following numbers: from $r = R_\odot$ to $r = 2\ R_\odot$, the density ρ decreases by a factor of approximately 10^3, while the area of a plume increases by roughly $(10^3)^{1/2}$. Consequently, the kinetic energy density, $\rho V^2/2$, remains roughly constant over this height range, while the magnetic energy density, $B^2/2\mu$ drops by roughly a factor of 10^3. This may explain why the plume properties remain distinct from those of the interplume gas up to about $r = 2\ R_\odot$ and then start to merge. As far as the actual interaction is concerned, it may be enhanced by, e.g., the Kelvin-Helmholtz instability, which can act at the boundary between two streams with sufficiently different speeds. In addition, electron collisions may not be sufficient at heights $\geq 2.0\ R_\odot$ to keep the different species in equilibrium. Consequently, plume species are heated and accelerated differently and rapidly as the density drops sharply with height. This may not be the case below this altitude, where the density is high enough to keep all species in equilibrium, contrasting interplume regions where the (electron) density is smaller, allowing for the plasma equilibrium to break down at lower altitudes, and thus for the plasma to become hotter and faster than in plume regions.

We find that observed profile shapes, line widths, and total intensities of the O VI doublet and of Lyα are better reproduced when the influence of appropriate plumes is included. In particular, the intensity ratios of the O VI doublet below $1.5\ R_\odot$ are smaller when the plume contribution is taken into account. This is due to the density enhancement in the plume region. This result is in disagreement with the interpretation preferred by Gabriel et al. (2003, 2005), that such a reduction in the ratio is due to the Doppler dimming effect, which would imply a higher outflow speed in plumes than in interplume regions. In our analysis, such high outflow speeds in the plumes produce synthetic profiles whose narrow component is Doppler shifted toward a profile wing, in contrast to the observations.

It is noteworthy that including polar plumes increases the agreement of the computed profiles with the observed ones and with critical parameters like line width or O VI line ratio, even if no anisotropy in the temperature (or turbulence velocity) is included in the computations. Note that the properties of the plumes were constrained basically using the line profile shape only, and the quantitative comparison with the line parameters and ratio was only carried out later. This strengthens the thesis put forward by Raouafi & Solanki (2004, 2006) that there is no compelling need for large anisotropies in temperature in coronal holes, based on published UVCS data.

Note that we have not tried to optimally reproduce the observed quantities by carrying out an exhaustive search in parameter space. Thus, the obtained results can possibly be improved further by applying a χ^2 minimization procedure to fit the line profiles.

Plumes with footpoints within 10°–15° of the pole display significant narrow components even at altitudes above $\approx 2.5\ R_\odot$, contrary to the observations. EIT images during the solar minimum, together with high-sensitivity magnetograms from SOLIS, show evidence supporting the hypothesis that plumes originate away from the pole. This subject will be studied in detail in a subsequent paper.

The authors would like to thank Craig DeForest for constructive comments and criticisms that greatly improved the manuscript, and John Raymond for helpful discussions. The NSO is operated by the Association of Universities for Research in Astronomy, Inc., under cooperative agreement with the National Science Foundation. N. E. R.'s work is supported by NSO and the NASA grant NNH05AA12I.

REFERENCES

Ahmad, I. A., & Webb, D. F. 1978, Sol. Phys., 58, 323
Ahmad, I. A., & Withbroe, G. L. 1977, Sol. Phys., 53, 397
Allen, M. J. 1994, Ph.D. thesis, Stanford Univ.
Banaszkiewicz, M., Axford, W. I., & McKenzie, J. F. 1998, A&A, 337, 940
Bohlin, J. D., Purcell, J. D., Sheeley, N. R., Jr., & Tousey, R. 1975a, BAAS, 7, 356
Bohlin, J. D., Sheeley, N. R., Jr., & Tousey, R. 1975b, in Space Research XV, ed. M. J. Rycroft (Berlin: Akademie), 651
Brueckner, G. E., et al. 1995, Sol. Phys., 162, 357
Cranmer, S. R., et al. 1999, ApJ, 511, 481
DeForest, C. E., Hoeksema, J. T., Gurman, J. B., Thompson, B. J., Plunkett, S. P., Howard, R., Harrison, R. C., & Hassler, D. M. 1997, Sol. Phys., 175, 393
DeForest, C. E., Lamy, P. L., & Llebaria, A. 2001a, ApJ, 560, 490
DeForest, C. E., Plunkett, S. P., & Andrews, M. D. 2001b, ApJ, 546, 569
Delaboudiniere, J.-P., et al. 1995, Sol. Phys., 162, 291
Del Zanna, L., Hood, A. W., & Longbottom, A. W. 1997, A&A, 318, 963
Domingo, V., Fleck, B., & Poland, A. I. 1995, Sol. Phys., 162, 1
Doyle, J. G., Keenan, F. P., Ryans, R. S. I., Aggarwal, K. M., & Fludra, A. 1999a, Sol. Phys., 188, 73
Doyle, J. G., Teriaca, L., & Banerjee, D. 1999b, A&A, 349, 956
Fisher, R. A., & Guhathakurta, M. 1995, ApJ, 447, L139
Gabriel, A. H., Abbo, L., Bely-Dubau, F., Llebaria, A., & Antonucci, E. 2005, ApJ, 635, L185
Gabriel, A. H., Bely-Dubau, F., & Lemaire, P. 2003, ApJ, 589, 623
Giordano, S., Antonucci, E., Noci, G., Romoli, M., & Kohl, J. L. 2000, ApJ, 531, L79
Giordano, S., et al. 1997, in Fifth *SOHO* Workshop, The Corona and Solar Wind Near Minimum Activity, ed. E. Wilson (ESA SP-404; Oslo: ESA), 413
Gopalswamy, N., Schmahl, E. J., & Kundu, M. R. 1992, in First *SOHO* Workshop, Observations of Stationary Radio Sources, ed. C. Mattok (Paris: ESA), 113
Habbal, S. R. 1992, Ann. Geophys., 10, 34
Harvey, J. W. 1965, ApJ, 141, 832
Hassler, D. M., Dammasch, I. E., Lemaire, P., Brekke, P., Curdt, W., Mason, H. E., Vial, J.-C., & Wilhelm, K. 1999, Science, 283, 810
Hassler, D. M., Wilhelm, K., Lemaire, P., & Schuehle, U. 1997, Sol. Phys., 175, 375

Kohl, J. L., et al. 1995, Sol. Phys., 162, 313
———. 1997, Sol. Phys., 175, 613
———. 1999, ApJ, 510, L59
Koutchmy, S. 1977, Sol. Phys., 51, 399
Lindblom, J. F. 1990, Ph.D. thesis, Stanford Univ.
Munro, R. H., & Jackson, B. V. 1977, ApJ, 213, 874
Newkirk, G. Jr., & Harvey, J. 1968, Sol. Phys., 3, 321
Raouafi, N.-E., Harvey, J. W., & Solanki, S. K. 2006, CD-ROM, in Proc. *SOHO*-17 Workshop: 10 Years of *SOHO* and Beyond, ed. H. Lacoste (ESA SP-617; Noordwijk: ESA)
Raouafi, N.-E., & Solanki, S. K. 2004, A&A, 427, 725
———. 2006, A&A, 445, 735
Saito, K. 1958, PASJ, 10, 49
———. 1965, PASJ, 17, 1
Saito, K., & Tanaka, Y. 1957a, PASJ, 9, 106
———. 1957b, PASJ, 9, 210
Teriaca, L., Poletto, G., Romoli, M., & Biesecker, D. A. 2003, ApJ, 588, 566
van de Hulst, H. C. 1950, Bull. Astron. Inst. Netherlands, 11, 150
Walker, A. B. C., DeForest, C. E., Hoover, R. B., & Barbee, T. D. W. 1993, Sol. Phys., 148, 239
Walker, A. B. C., Jr., Lindblom, J. F., Barbee, T. W., Jr., & Hoover, R. B. 1988, Science, 241, 1781
Wang, Y.-M. 1994, ApJ, 435, L153
———. 1998, ApJ, 501, L145
Wang, Y.-M., & Sheeley, N. R., Jr. 1995, ApJ, 452, 457
Widing, K. G., & Feldman, U. 1992, ApJ, 392, 715
Wilhelm, K. 2006, A&A, 455, 697
Wilhelm, K., Dammasch, I. E., Marsch, E., & Hassler, D. M. 2000, A&A, 353, 749
Wilhelm, K., Marsch, E., Dwivedi, B. N., Hassler, D. M., Lemaire, P., Gabriel, A. H., & Huber, M. C. E. 1998, ApJ, 500, 1023
Wilhelm, K., et al. 1995, Sol. Phys., 162, 189
Woo, R., & Habbal, S. R. 1999, ApJ, 510, L69
Woo, R., Habbal, S. R., Howard, R. A., & Korendyke, C. M. 1999, ApJ, 513, 961
Young, P. R., Klimchuk, J. A., & Mason, H. E. 1999, A&A, 350, 286
Zirker, J. B. 1977, Rev. Geophys. Space Phys., 15, 257